Concentric Split-Ring Resonator Microwave Microplasma Generation at Off-Resonant Frequencies

Roberto A. Dextre¹⁰, Toyofumi Yamauchi, Kurt A. Polzin¹⁰, Senior Member, IEEE, and Kunning G. Xu¹⁰, Member, IEEE

Abstract—The driving frequency of a microstrip concentric split-ring resonator (CSRR) was varied to determine how the generated microplasma changes as a function of frequency, specifically at off-resonant frequencies. The microplasmas were generated in argon at 1 torr, using a forward microwave power level of approximately 10 W. The resonant frequency was experimentally found to be 796 MHz, and measurements were obtained at this frequency and ±10 MHz from resonance. Double Langmuir probe measurements were performed on a 2-D grid, parallel to the surface of the device, to obtain plasma density and electron temperature maps. The results show multiple peaks in plasma properties due to electromagnetic coupling with the nested ring. The electron temperature above the primary discharge gap is 8.5 eV at 786 MHz, 9.5 eV at 796 MHz, and 7.6 eV at 806 MHz. A secondary discharge is also observed above the secondary nested ring gap, and the plasma in this region is generally of lower temperature. The off-resonant operation resulted in lower temperatures and densities, with larger decreases in the 806 MHz case. The electromagnetic response of the device was modeled to understand the electric field in the discharge gap. The modeling revealed that the electric field vectors at the bounds of the discharge gap point in the opposite directions for the 786 and 796 MHz cases, increasing the electric field in the gap, but these vectors point in the same direction for the 806 MHz case, decreasing the electric field.

Index Terms—Langmuir probe, microplasma, split-ring resonator (SRR).

I. INTRODUCTION

MICROSTRIPS are thin-stripped conductors fabricated on a substrate with a high dielectric constant. Microwave signals can be made to propagate in a microstrip.

A microstrip may be cut along the conductor so that there is a gap in the strip, and for certain gap locations, the microstrip will act as a resonator with a strong electric field forming at the gap. These resonators can be configured either as straight-line conductive paths (linear resonators) or as ring-shaped paths [split-ring resonators (SRRs)]. If the field in the resonator gap is sufficiently strong, it can ionize the surrounding gas and generate microplasma. Microplasmas are small-scale discharges, typically millimeter scale or smaller. Past applications for microplasmas include bacteria sterilization [1], [2], treatment of skin [3], surface activation [2], nanomaterial synthesis [4], and thin film coating [5].

In previous studies employing an array of linear resonator strips, where only one strip was powered, it was observed that power coupled to neighboring unpowered strips [6]. The combination of microwave energy coupling into the neighboring strips and the ignition of the first powered resonator resulted in the formation of a line of discrete microplasma sources at the gaps in neighboring, unpowered strips.

SRRs and concentric SRR (CSRRs) are microstrip-geometry devices that have been studied heavily in the metamaterial field for their interesting electromagnetic behavior. The CSRR is similar to the array of linear resonators, except that the unpowered split rings are concentrically nested within the powered SRR. While past research on CSRRs has focused on the intraring spacing and subsequent electromagnetic resonance behaviors [6], [7], this article investigates the CSRR as a microplasma source with

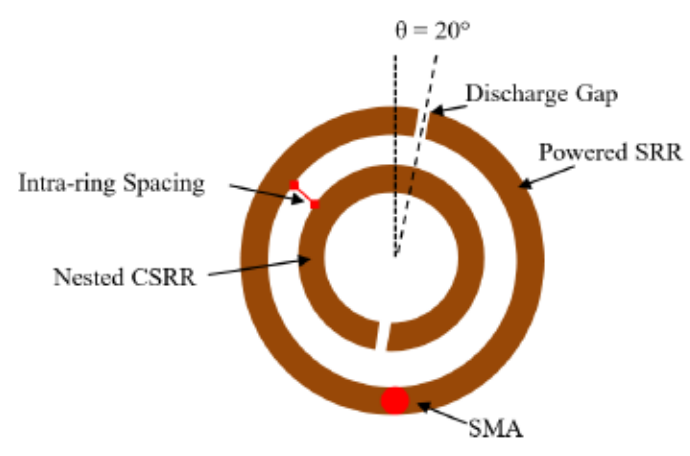


Fig. 1. Schematic of CSRR design.

transmitters operating in the L- or S-bands. This would remove the need for a dedicated power system to drive the thruster. However, since the actual assigned frequency for a given satellite may vary and it is unlikely each CSRR-based thruster would be custom-designed for each satellite, the CSRR would have to be capable of operating at off-resonant frequencies. Consequently, it is of interest to determine how the CSRR plasma behaves for off-resonant frequencies, providing insight into whether a resonant CSRR must be designed specifically for each given satellite or if a single design can be used over a broad range of input frequencies.

II. EXPERIMENTAL DESCRIPTION

A. CSRR Device Characteristics

An RT/Duroid 6010 laminate sheet (\sim 10.2 dielectric constant) with copper cladding on both sides (32- μ m thick) is utilized in the fabrication of the CSRR. The CSRR consists of a powered outer SRR with a nested electrically isolated concentric SRR as shown in Fig. 1. The conducting rings are produced on one side of the substrate, while the back plane is unmodified. The center conductor of an SubMiniature version A (SMA) connector is soldered to the outer ring, while the outer, grounded portion of the connector is soldered to the back plane.

The CSRRs were fabricated using photolithography and wet etching techniques. The widths of the rings are nominally fabricated to be 1.5 mm and the design frequency for the outer ring is 700 MHz. The nested ring is sized to be the first harmonic of the design frequency, 1400 MHz. The intraring spacing was set at 1 mm based on fabrication limits. The mean circumference $l_{\rm circ}$ of the SRR is designed to be half the wavelength at the driving frequency f

$$l_{\rm circ} = \frac{\lambda}{2} = \frac{c}{2f\sqrt{\varepsilon_r}} \tag{1}$$

where c is the speed of light, λ is the wavelength, and ε_r is the relative permittivity of the substrate. The microwave signal delivered through the SMA connector propagates through a ring producing an oscillating electric field that has a peak value at the discharge gap of the SRR [9]. The amplitude of the oscillating electric field is sufficient to ionize the gas at the gap. A phase offset angle, θ , is assigned to ensure

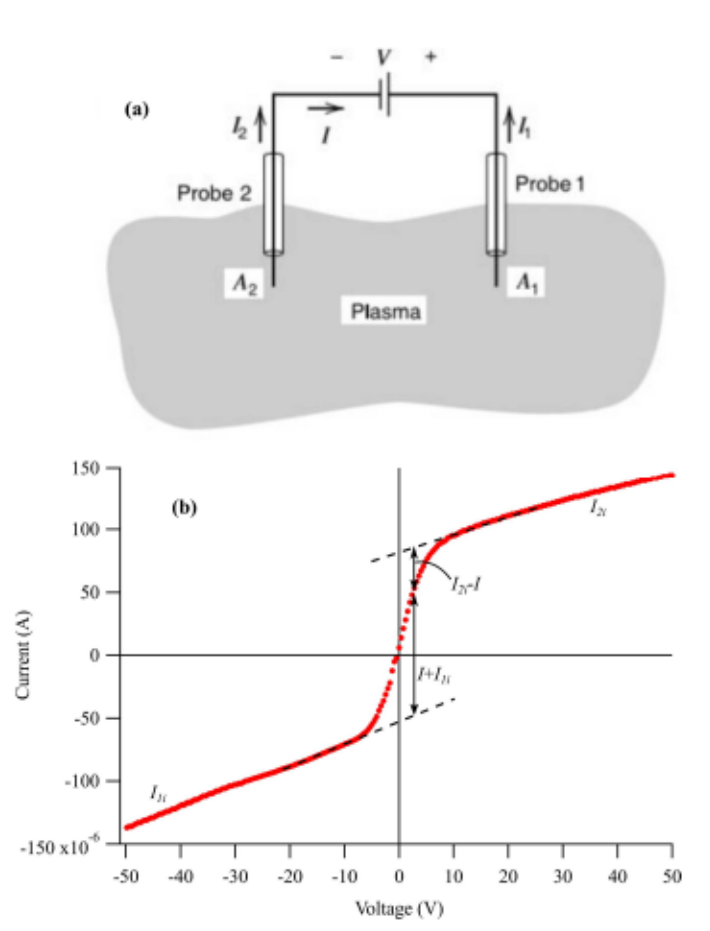


Fig. 2. (a) Schematic of a double probe showing the applied voltage and current sign conventions from [11]. (b) Sample voltage and current trace from the CSRR data showing locations of relevant currents for double probe calculations.

the field strength peak is at the gap. The location of the secondary discharge gap in the nested ring is 180° from the powered ring discharge gap. Both inner and outer rings have 500-μm wide gaps. As the electromagnetic radiation is coupled from the outer ring into the inner ring, a signal propagates to the secondary discharge gap of the nested ring resulting in the formation of a secondary ionization point. The CSRR geometry was first theoretically sized using (1) for 700 MHz, based on the operating range of the experimental equipment. The theoretical geometry was then analyzed using ANSYS High Frequency Structure Simulator (HFSS) to simulate the electric fields. After fabrication, the CSRR was tested and the resonant frequency, based on minimized voltage standing wave ratio (VSWR), was experimentally found to be 796 MHz. Lastly, the HFSS simulation was performed again using the measured resonant frequency of 796 MHz and tested at the off-resonant frequencies of 786 and 806 MHz. The modeling results presented in this article are for this final set of simulations.

B. Langmuir Probe Diagnostic

A double Langmuir probe, shown schematically in Fig. 2(a), was used to measure the electron temperature and plasma number density of the microplasma at discrete locations in

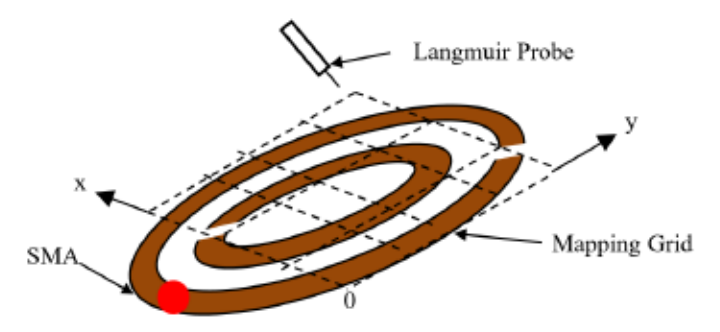


Fig. 3. CSRR rendering with a notional gridded mapping (not to scale) showing point for double Langmuir probe data acquisition. The point spacing results in a 6 × 6 grid for a total of 36 locations.

the discharge. The probe was fabricated using two tungsten wires covered by an alumina shield with exposed tips at the end. The tips have a diameter of 0.127 mm, a length of 2 mm, and the end of the tips are positioned to be \sim 4 mm above the surface of the CSRR. An external bias voltage was applied to the Langmuir probes with the voltage applied to each tip swept from -50 to 50 V. The current as a function of voltage was measured to yield an I-V curve (shown notionally in Fig. 2(b), which was analyzed to determine the plasma properties [10].

The probe was positioned at discrete locations in a 2-D plane, parallel to the face of the CSRR, to measure microplasma properties over a grid of locations. This grid is shown in an isometric view superimposed over the CSRR in Fig. 3. Each x-axis step was 5.6 mm while each y-axis step was 4.1 mm with the origin at the lower right corner. The matrix was built to ensure measurement at both discharge gaps of the device, while keeping the probe from interfering with or impinging upon the SMA connector.

The double Langmuir probe is considered to be in the collisionless regime, if the ratio of the Debye length λ_D to the ion-neutral collisional mean-free path of the plasma λ_{mfp} is less than unity [12]

$$\alpha_c = \frac{\lambda_D}{\lambda_{\text{mfp}}} < 1.$$
 (2)

The ion-neutral collisional mean-free path can be determined as $\lambda_{\rm mfp} = 1/(n\sigma)$, where n is the neutral number density and σ is the cross section for argon ion-neutral collisions [13]. The neutral density can be obtained from the ideal gas equation of state, and the argon ion-neutral collision cross section is obtained from [14]. For the pressures and plasma properties in this article, the plasma α_c is between 2.5×10^{-4} and 1.0×10^{-3} , allowing us to assume that the plasma is in the collisionless regime [10].

For the double probe shown in Fig. 2(a), the current collected by the each of the two probe tips of equal area as a function of the applied voltage at each tip is given as

$$i_1 = i_0 \left(1 - e^{\frac{\epsilon(V_1 - V_F)}{(kT_e)}} \right) \tag{3}$$

$$i_2 = i_0 \left(1 - e^{\frac{\epsilon(V_2 - V_F)}{(kT_c)}} \right) \tag{4}$$

where $|I_{1i}| = |I_{2i}| = i_0$ are the ion saturation currents in Fig. 2(b), e is the elementary charge, V_F is the floating

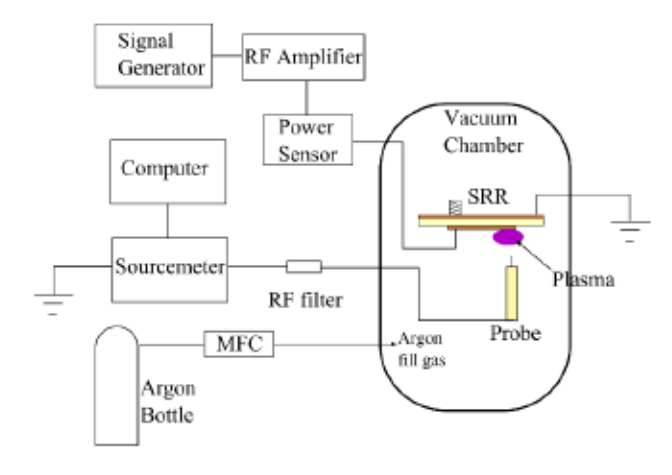


Fig. 4. Diagram of the experimental setup. MFC.

potential, k is Boltzmann's constant, and T_e is the electron temperature. The currents collected by the probes are constrained, such that $i_1 + i_2 = 0$, while the voltages applied to each probe tip satisfy the relationship, $V_2 = V_1 - V$. Manipulation of the current collection (3) and (4) under these constraints allows us to write the double probe I-V characteristic as

$$i_1 = i_0 \tanh \left(eV/(2kT_e) \right). \tag{5}$$

Finding the slope of the I-V characteristic at V=0 permits us to solve for the electron temperature as

$$\frac{kT_e}{e} = i_0 / \left(2 \left. \frac{di_1}{dV} \right|_{V=0} \right). \tag{6}$$

The ion saturation current based on Bohm's criteria is

$$i_0 = \exp(-1/2)en_e A \sqrt{\frac{kT_e}{m_i}}$$
 (7)

where m_i is the ion mass. With the electron temperature already calculated from the data and the ion saturation current known through measurement, this equation can be rearranged to yield the number density in terms of known quantities as

$$n_e = i_0 / \left[\exp(-1/2)eA\sqrt{\frac{kT_e}{m_i}} \right]. \tag{8}$$

C. Experimental Setup

A schematic of the experimental setup is shown in Fig. 4. The CSRR was tested at its experimental resonant frequency (796 MHz) and at frequencies of 10 MHz above and below resonance (786 and 806 MHz). The preamplified input power from a signal generator, which was set to -15.0 dBm, drives a +55-dB gain RF amplifier. The amplifier signal goes into a Bird 7020 power sensor that measured the forward and reflected power of the circuit. The resonant frequency of 796 MHz was experimentally found by varying the input frequency until the VSWR was minimized. The total forward power sent to the device during operation was ~10 W. Bottled research-grade argon gas was metered with an MKS mass flow controller (MFC). The chamber pressure was 1 torr argon for all experiments and was measured with an MKS Baratron

TABLE I

CSRR Powered and Nested Ring Electric Field Intensities
Within Discharge Gaps for Assigned Frequency

Frequency (MHz)	Powered Ring Gap E-Field (V/m)	Nested Ring Gap E-Field (V/m)
786	3.11 x 10 ⁴	3.89 x 10 ³
796 (resonant)	3.37 x 10 ⁴	4.22 x 10 ³
806	2.99 x 10 ⁴	3.75 x 10 ³

capacitance manometer. A low-pass RF filter with a cutoff of 100 MHz was placed in the Langmuir probe circuit to remove RF signals in the probe data. A Labview-controlled Keithley 2410 sourcemeter was used to apply voltage to the double probe tips and to measure the collected current.

The systematic error sources include the probe area ($\pm 10\%$) and sourcemeter voltage and current (±0.03%). The random errors in measurements are addressed by averaging multiple measurements. The Labview program sweeps the probe voltage from -50 to 50 V and performs five current measurements at each voltage to produce an averaged current reading. Three voltage sweeps are performed at each location, and these are then averaged to produce an average I-V curve used in our analysis. The largest potential source of error is in the probe analysis itself. The equations used and the assumptions involved, including the assumptions of a Maxwellian electron energy distribution and probes of exactly the same area, result in errors on the calculated temperatures and densities of ±50% relative to the true values. As the same physical probe and analysis techniques are applied to all measurements, the relative error between different measurement points should be smaller, mainly due to random sources of measurement variation.

III. MODELING AND MEASUREMENTS

A. Simulations

ANSYS HFSS was used to model the electric field behavior as microwave energy is applied to the CSRR. Fig. 5 shows the electric field intensity and the corresponding vector plots from the HFSS simulations at 10 W for a frequency range from 786 to 806 MHz. The frequency range was selected based on the ±10 MHz range around the experimentally determined resonant frequency of 796 MHz. The electric field maps show the field intensity peaks at the discharge gaps of both rings, while the vector plots show the directional behavior of the electric field as it propagates around the primary and secondary rings. Fringing electric fields are observed along the edges of an antenna, in this case, the primary outer ring. Electric fields are subsequently produced in any nearby conducting material owing to the fringing electric fields [15] as they couple power from the powered outer ring into the nested ring [16].

Table I lists the maximum electric field intensities within the discharge gaps as a function of frequency obtained from simulations of the coupled powered and nested rings. As expected, the outer, directly driven ring exhibits a significant electric field at the gap. The electric field in the nested ring is also high, although it is about an order of magnitude lower than the field in the powered ring gap. While the formation of a

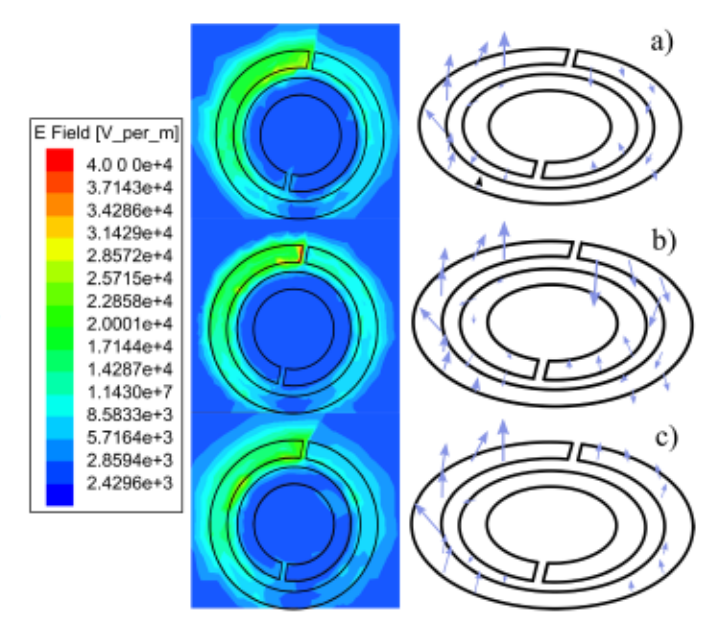


Fig. 5. CSRR electric field intensity simulations with the outer, powered resonator driven at (a) 786 MHz (-10 MHz from resonance), (b) 796 MHz (resonant frequency), and (c) 806 MHz (+10 MHz from resonance).

plasma is outside the scope of the model, the field is maximum at the resonant frequency of 796 MHz, which suggests that if a plasma is formed at all three frequencies, as shown in Table I, the plasma formed at 786 and 806 MHz should both have lower densities than the resonant case. Compared to the resonant case, the 786 MHz case exhibits a smaller reduction in the peak electric fields for both rings relative to the 806 MHz case. Consequently, if a plasma forms in all cases, we would expect the plasma density in the 806 MHz case to be smaller than the density in the 786 MHz case.

The automesher in HFSS was used for the simulation, as the model was primarily used to help design and resonators. The automesher performs automesh refinement on areas of the simulation with high gradients in the electromagnetic field. The default convergence criteria for the HFSS module is 2%. This was sufficient to generate insights into the operation of a CSRR and the trends on field maximization as a function of frequency.

An interesting observation from the 806 MHz vector plot in Fig. 5(c) is that the electric field vectors in the outer ring on both sides of the gap are in the same direction. This is in comparison to the other two simulation results, where opposing vectors appear within the conductors adjacent to the discharge gap. This result helps explain the lower field intensity in the discharge gap in the 806 MHz case when compared to 786 MHz case.

The magnetic field induced by currents driven in the CSRR configuration was also calculated, and for completeness they are shown in Fig. 6 for the resonant frequency case. The magnetic field lines wrap around the outer conductor, and in the middle of the device, the field aligns with the center axis of the CSRR geometry. As the frequency is increased, the average magnetic field strength increases, with this increase quantified in Table II, where we provide the magnetic field strength at the center axis as a function of frequency.

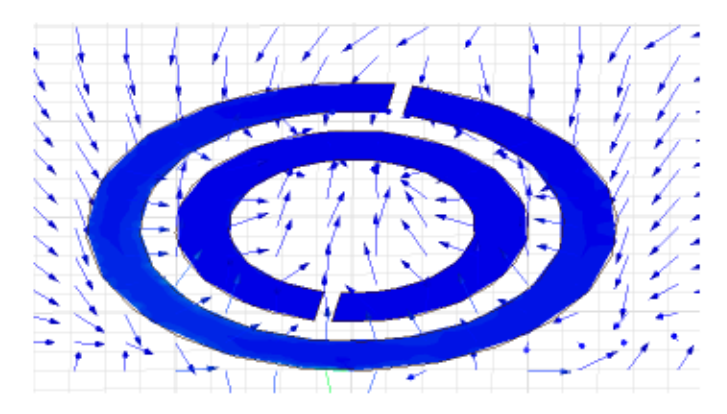


Fig. 6. CSRR magnetic field intensity simulations with the outer, powered resonator driven at 796 MHz (resonant frequency).

TABLE II

MAGNETIC FIELD STRENGTH ON THE CENTER AXIS OF THE CSRR
CONFIGURATION AS A FUNCTION OF DRIVING FREQUENCY

Frequency (MHz)	Magnetic Field Strength (G)
786	9.1
796	11.8
806	15.6

B. Electron Temperature Measurements

A plasma was produced in the CSRR at off-resonant frequencies down to 786 MHz and up to 806 MHz. Operation at higher and lower frequencies did not result in repeatable plasma generation, indicating that at constant input power there is a bandwidth limit on the frequencies at which a plasma can be realized. The electron temperature was determined at each of the three frequencies from the double Langmuir probe data, an example of which is shown in Fig. 2(b). Electron temperature data are shown in Figs. 7–9 for the lower off-resonant frequency of 786 MHz, the resonant frequency of 796 MHz, and the higher-off resonant frequency of 806 MHz, respectively. In these and subsequent figures, dashed lines are used to indicate the location of the two discharge gaps that were previously shown in the CSRR rendering of Fig. 3.

At 796 and 806 MHz, the electron temperature maps indicate two regions of higher temperature, corresponding to the locations of the two discharge gaps and indicating that secondary ignition was achieved in the gap of the nested ring. There are two peaks in the 786 MHz case as well, but the peak is offset from the primary discharge gap by approximately 5 mm in the x-direction. In all cases, the electron temperature at the nested ring gap is lower than that measured at the powered ring gap. The electron temperature of the resonant case is overall higher, including minimum and maximum temperatures in the domain than are greater than for the off-resonant frequency cases. The resonant (796 MHz) case temperature varies from 7.0 to 9.6 eV, while for the 786 and 806 MHz cases these temperature ranges are 6.5–9.3 and 6.3-8.3 eV, respectively. The electron temperatures at the powered ring gaps are measured as 8.5 eV at 786 MHz (-10 MHz from resonance), 9.5 eV at 796 MHz (resonance), and 7.6 eV at 806 MHz (+10 MHz from resonance). These

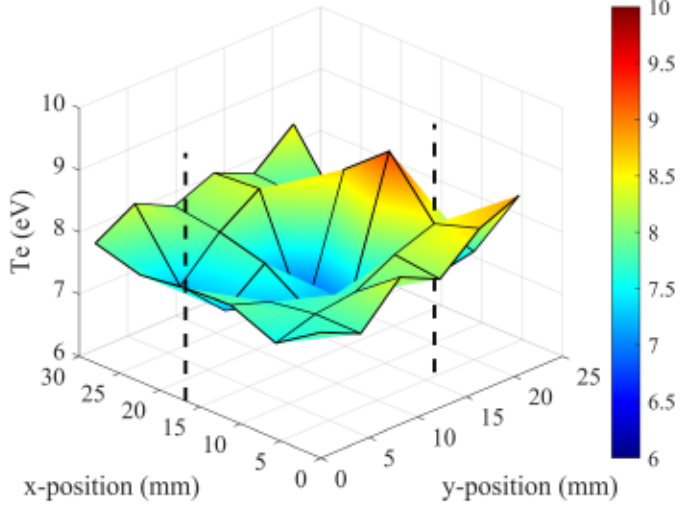


Fig. 7. CSRR measured electron temperatures at 786 MHz with $\sim \! \! 10$ W of forward power.

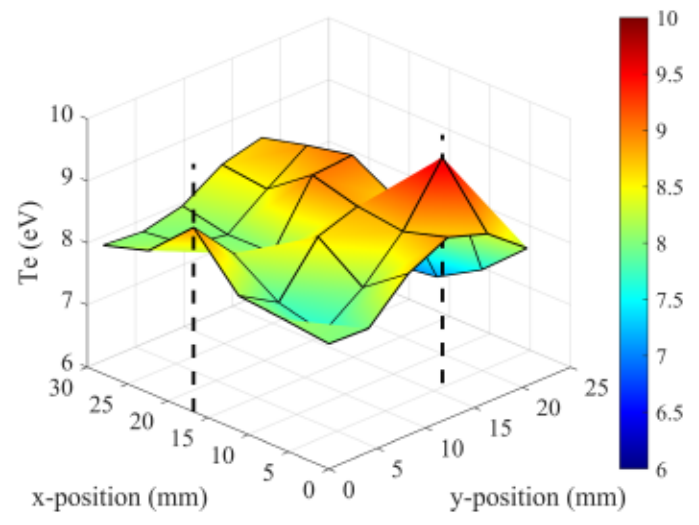


Fig. 8. CSRR measured electron temperatures at 796 MHz (resonant frequency) with ~10 W of forward power.

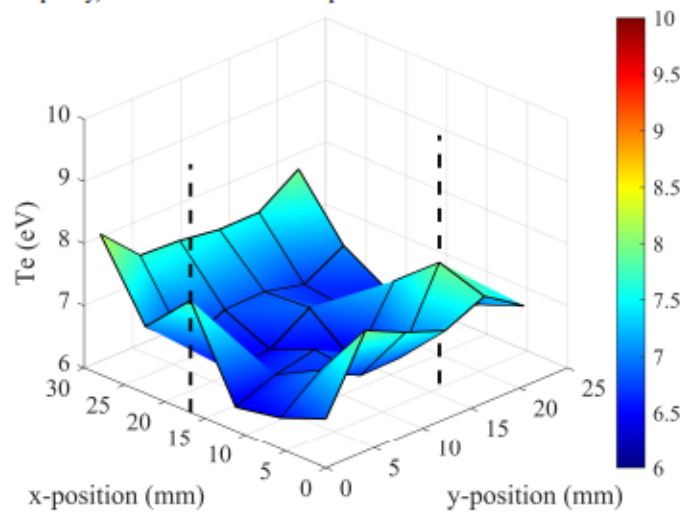


Fig. 9. CSRR measured electron temperatures at 806 MHz with $\sim\!\!10$ W of forward power.

decreases in the electron temperature for off-resonant operation correlate with the electric field strengths found through the HFSS simulations, where the electric field in the discharge gap was a maximum at resonance, reduced from the maximum at 786 MHz, and a minimum value at 806 MHz.

C. Number Density Measurements

The number densities calculated from the double probe measurements are shown in Figs. 10–12 for 786, 796, and 806 MHz, respectively. The peaks in number density favor the radial centerline of the device (along the $\theta=0^{\circ}$, 180° line in Fig. 1), instead of the discharge gaps where the larger electric field is located. These peak densities between each frequency varied from 1.10×10^{17} , 1.15×10^{17} , and 1.02×10^{16} /m³ for 786, 796, and 806 MHz, respectively.

IV. DISCUSSION

The CSRR microwave gap discharge can be considered a medium-pressure capacitively coupled plasma. The electron temperature plots show the high temperature electrons are generally at or near the two discharge gaps, implying that the electrons are gaining energy from high electric fields present at those locations. As the electrons diffuse outward, they lose energy through inelastic collisions. The density data indicate that the majority of the ion population is located in a lower temperature region along the radial centerline of the CSRR. Separation of the peak temperature and number density is often observed in RF-sustained plasmas [17]-[21]. Ions created at the gap move away from that location at the ion acoustic velocity. The energetic electrons may also provide additional ionization as they diffuse outward from the discharge gap. However, if this was simply a case of isotropic ion motion and energetic electron diffusion, then a ring of higher plasma density should form around each of the gaps. Instead, the data show the radial centerline of the CSRR being a favored location for the elevated number density.

The trends in electron temperature and number density as a function of frequency, namely that these are maximized for the resonant case of 796 MHz and a minimum for operation at 806 MHz, can be attributed to the discharge gap electric field strength being maximized in the resonant case and minimized (for the cases tested) at 806 MHz. As previously noted, at 806 MHz, our modeling indicates that the electric fields on either side of the powered-ring discharge gap would be in the same direction.

An ideal SRR would be comprised of a single thin conductor of the appropriate path length to support the resonant frequency given by (1), resulting in a commensurate maximum electric field in the gap. The theoretical design frequency for the outer powered ring in this article was 700 MHz, corresponding to a circumference and mean diameter of 6.71 and 2.14 cm, respectively. These values were used to set the average circumference and diameter of the outer powered ring, as shown by the line through the middle of the circuit trace, schematically shown in the left frame of Fig. 13.

However, the ring also has a finite width of 1.5 mm, which is set by the fabrication process. In the left frame of Fig. 13, there are two other circumferences drawn corresponding to the maximum and minimum diameters of a path that is still completely contained within the ring. These outer and inner

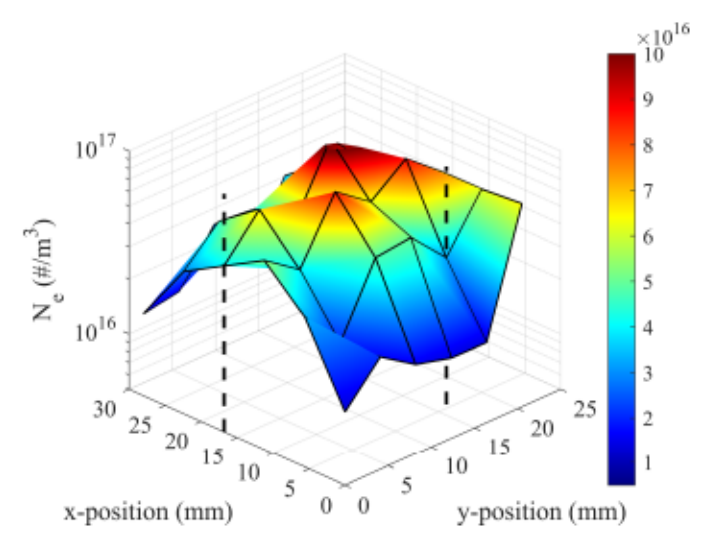


Fig. 10. CSRR measured number density at 786 MHz with ~10 W of forward power.

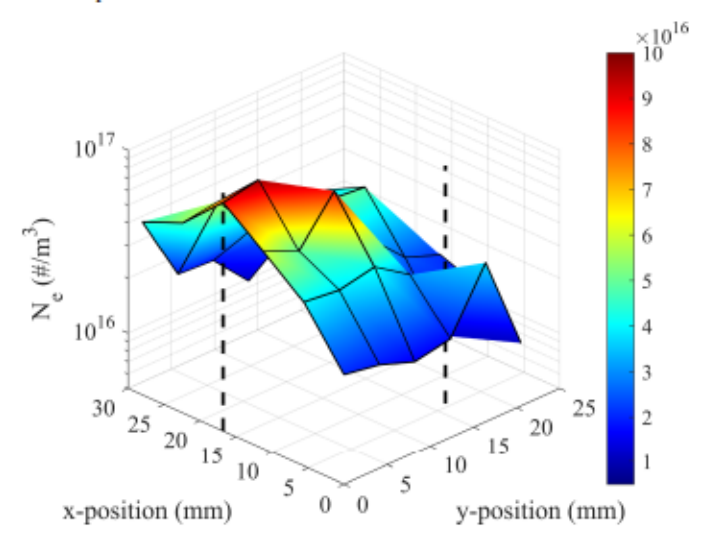


Fig. 11. CSRR measured number density at 796 MHz (resonant frequency) with \sim 10 W of forward power.

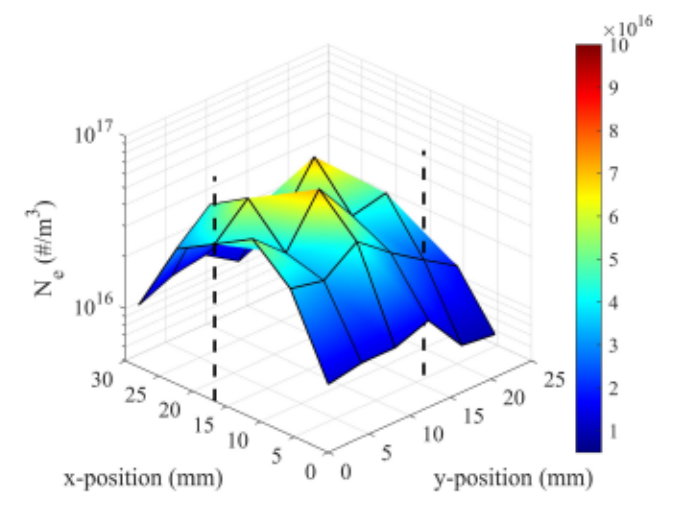


Fig. 12. CSRR measured number density at 806 MHz with $\sim \! \! 10$ W of forward power.

diameters are 2.29 and 1.99 cm, respectively, and they correspond to circumferences of 7.19 and 6.25 cm, respectively.

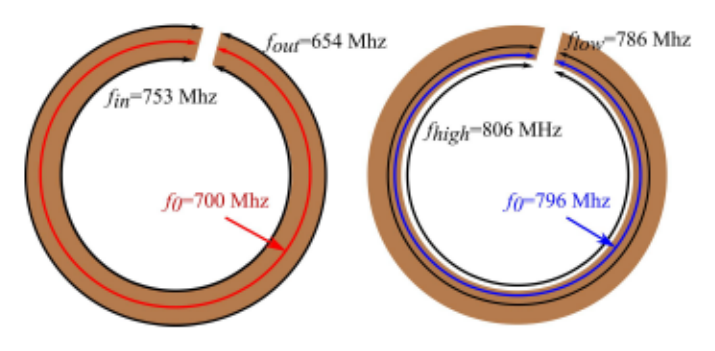


Fig. 13. (Left) Schematic representation of the circumferences corresponding to the path lengths in an SRR that would support resonant operation at the frequencies listed (for inner, average, and outer diameters of 1.99, 2.14, and 2.29 cm, respectively). (Right) Notional representation of the circumferences corresponding to the path lengths in the outer, powered ring of the tested CSRR showing those the paths for 786 and 796 MHz lying within the conductor and the path for 806 MHz lying outside the conductor.

Using (1), the resonant frequencies corresponding to those circumference values are 654 MHz for the outer diameter path and 753 MHz for the inner diameter path. Consequently, we could reasonably suspect that applying RF power bounded by these frequency values could result in favorable electric fields being generated at the gap to support plasma formation (specifically, electric field vectors in the opposite directions on either side of the gap).

As we noted from our data, the resonant frequency of the real device was experimentally determined to be 796 MHz. The 96 MHz shift in resonance relative to the design frequency is likely driven by a combination of three factors: fabrication tolerances, substrate dielectric variation, and electromagnetic coupling to the inner, nested ring. Based on the discussion above regarding the left frame of Fig. 13, we set forth the following notional reasoning for why the electric fields point in the opposite directions at the gap in the 796 and 786 MHz cases, but not in the 806 MHz case. Specifically, we postulate that resonant frequency circumferences for 796 and 786 MHz in the as-tested CSSR are still completely contained within the conductor, but the circumference corresponding to the higher frequency, 806 MHz, falls outside the conductor. These circumferences are notionally shown in the right frame of Fig. 13. As a consequence, the electric fields generated at the gap are favorable (opposite directions on either side of the gap) in the 796 and 786 MHz cases, and less favorable (same direction on either side of the gap) in the 806 MHz case.

V. CONCLUSION

In this article, a CSRR for micropropulsion applications was tested at resonant and off-resonant frequencies to understand how the microplasma properties change as a function of operating frequency. Resonant frequency operation at 796 MHz produced the highest electron temperature and plasma density. The electron temperature decreased as the frequency was varied to off-resonance values, with the 786 MHz case (-10 MHz from resonance) exhibiting a smaller decrease in temperature compared to the 806 MHz case (+10 MHz from resonance). The scaling is due to the electric field in the discharge gap being largest in the resonant case and successively smaller in

the 786 and 806 MHz cases, respectively. Measurement of the electron temperature and plasma density in three dimensions, using a finer grid mapping, could aid in better understanding the transport of energetic electrons and plasma ions from the gap. Such a mapping is also necessary if a CSRR is to be integrated into any future micropropulsion system, as it will help to understand the plasma conditions as it enters a thruster (for example, in a microion thruster where the plasma properties at the inner screen grid dictate the ion flux into the ion optics and thus the performance of the engine). Testing has demonstrated that a CSRR driven by the onboard telecommunications transmitter power source and integrated into a thruster could be feasible, and that such a device does support some range of operating frequencies. The results point toward a path by which the device might be designed for operation over a broad frequency range. The effect that the coupled inner ring has on the resonant frequency of the device is not well understood or modeled in this article. Therefore, further studies on this topic is recommended.

ACKNOWLEDGMENT

Roberto A. Dextre would like to thank the University of Alabama in Huntsville for its support, and the Mechanical and Aerospace Engineering Department, the Propulsion Research Center, and the Nano and Micro Devices Center for hosting the research and development of the microplasma source.

REFERENCES

- K. Shimizu, M. Blajan, and T. Kuwabara, "Removal of indoor air contaminant by atmospheric microplasma," *IEEE Trans. Ind. Appl.*, vol. 47, no. 6, pp. 2351–2358, Nov. 2011.
- [2] A. Mizuno, "Recent progress and applications of non-thermal plasma," Int. J. Plasma Environ. Sci. Technol., vol. 3, no. 1, pp. 1–7, 2009.
- [3] Y. C. Hong and H. S. Uhm, "Microplasma jet at atmospheric pressure," Appl. Phys. Lett., vol. 89, no. 22, Nov. 2006, Art. no. 221504.
- [4] D. Mariotti and R. M. Sankaran, "Microplasmas for nanomaterials synthesis," J. Phys. D, Appl. Phys., vol. 43, no. 32, Jul. 2010, Art. no. 323001.
- [5] F. Iza and J. Hopwood, "Split-ring resonator microplasma: Microwave model, plasma impedance and power efficiency," *Plasma Sources Sci. Technol.*, vol. 14, no. 2, pp. 397–406, May 2005.
- [6] Z.-B. Zhang and J. Hopwood, "Linear arrays of stable atmospheric pressure microplasmas," Appl. Phys. Lett., vol. 95, no. 16, Oct. 2009, Art. no. 161502.
- [7] P. Gay-Balmaz and O. J. F. Martin, "Electromagnetic resonances in individual and coupled split-ring resonators," J. Appl. Phys., vol. 92, no. 5, pp. 2929–2936, Sep. 2002.
- [8] F. Bilotti, A. Toscano, and L. Vegni, "Design of spiral and multiple split-ring resonators for the realization of miniaturized metamaterial samples," *IEEE Trans. Antennas Propag.*, vol. 55, no. 8, pp. 2258–2267, Aug. 2007.
- [9] R. A. Dextre and K. G. Xu, "Effect of the split-ring resonator width on the microwave microplasma properties," *IEEE Trans. Plasma Sci.*, vol. 45, no. 2, pp. 215–222, Feb. 2017.
- [10] P. R. Smy, "The use of langmuir probes in the study of high pressure plasmas," Adv. Phys., vol. 25, no. 5, pp. 517–553, Sep. 1976.
- [11] M. A. Lieberman and A. J. Lichtenberg, Principles of Plasma Discharges and Materials Processing, 2nd ed. Hoboken, NJ, USA: Wiley, 2005.
- [12] T. E. Sheridan and J. Goree, "Collisional plasma sheath model," Phys. Fluids B, Plasma Phys., vol. 3, no. 10, pp. 2796–2804, Oct. 1991.
- [13] D. M. Goebel and I. Katz, Fundamentals of Electric Propulsion: Ion and Hall Thrusters. Pasadena, CA, USA: Jet Propulsion Laboratory, 2008.
- [14] A. V. Phelps, "Cross sections and swarm coefficients for nitrogen ions and neutrals in n2 and argon ions and neutrals in ar for energies from 0.1 eV to 10 keV," J. Phys. Chem. Reference Data, vol. 20, no. 3, pp. 557-573, May 1991.

- [15] J.-S. Hong and M. J. Lancaster, "Couplings of microstrip square openloop resonators for cross-coupled planar microwave filters," *IEEE Trans. Microw. Theory Techn.*, vol. 44, no. 11, pp. 2099–2109, Nov. 1996.
- [16] F. Iza and J. A. Hopwood, "Low-power microwave plasma source based on a microstrip split-ring resonator," *IEEE Trans. Plasma Sci.*, vol. 31, no. 4, pp. 782–787, Aug. 2003.
- [17] R. F. Boivin, J. L. Kline, and E. E. Scime, "Electron temperature measurement by a helium line intensity ratio method in helicon plasmas," *Phys. Plasmas*, vol. 8, no. 12, pp. 5303–5314, Dec. 2001.
- [18] V. A. Godyak and R. B. Piejak, "Abnormally low electron energy and heating-mode transition in a low-pressure argon rf discharge at 13.56 MHz," Phys. Rev. Lett., vol. 65, no. 8, pp. 996–999, Aug. 1990.
- [19] P. A. Keiter, E. E. Scime, and M. M. Balkey, "Frequency dependent effects in helicon plasmas," *Phys. Plasmas*, vol. 4, no. 7, pp. 2741–2747, Jul. 1907
- [20] Y. Jeong et al., "Two-dimensional fluid simulation of large-scale, capacitively-coupled plasma discharge for display device processes," J. Nanosci. Nanotechnol., vol. 17, no. 11, pp. 8411–8417, Nov. 2017.
- [21] F. F. Chen, "Radiofrequency plasma sources for semiconductor processing," in Advanced Plasma Technology. 2007, pp. 99–115.



Toyofumi Yamauchi received the B.S. degree in aerospace engineering from the University of Alabama in Huntsville, Huntsville, AL, USA, in 2019. He is currently pursuing the Ph.D. degree in aerospace engineering at the University of Illinois at Urbana-Champaign, Urbana, IL, USA.

From 2016 to 2018, he was an Undergraduate Research Assistant with the Plasma and Electrodynamics Research Laboratory (Propulsion Research Center). His research interest includes the development of miniature ion thruster, the utilization of the

split ring resonator, and multimode propulsion system.



Kurt A. Polzin (Senior Member, IEEE) received the B.S. degree (summa cum laude) in aeronautical and astronautical engineering from The Ohio State University, Columbus, OH, USA, in 1999, and the Ph.D. degree from Princeton University, Princeton, NJ, USA, in 2006. He was previously a Propulsion Research Scientist in the Propulsion Research and Development Laboratory. He has been with NASA's George C. Marshall Space Flight Center, Huntsville, AL, USA, since 2004, and is currently the Space Systems Team Lead in the Advanced Concepts

Office, Huntsville, AL, USA.

Dr. Polzin is an Associate Fellow of the American Institute of Aeronautics and Astronautics (AIAA). He is the AIAA Southeast Regional Director and also a member of the AIAA Electric Propulsion Technical Committee. He was the Technical Chair of the 2013 International Electric Propulsion Conference (IEPC) held at George Washington University, Washington, DC, USA, and is a mission area Co-Chair for the Spacecraft Propulsion Subcommittee meetings of JANNAF (Joint Army-Navy-NASA-Air Force).



Roberto A. Dextre received the B.S. degree in mechanical and aerospace engineering from SUNY Binghamton, Binghamton, NY, USA, in 2012, and the M.S. and Ph.D. degrees in aerospace engineering from The University of Alabama in Huntsville, Huntsville, AL, USA, in 2014 and 2018, respectively.



Kunning G. Xu (Member, IEEE) received the B.S., M.S., and Ph.D. degrees in aerospace engineering from the Georgia Institute of Technology, Atlanta, GA, USA, in 2006, 2009, and 2012, respectively. He is currently an Associate Professor with the Mechanical and Aerospace Engineering Department, The University of Alabama in Huntsville, Huntsville, AL, USA. His research interests include plasma propulsion, plasma-assisted combustion, and atmospheric-pressure microplasma science and engineering.